This is the accepted manuscript made available via CHORUS. The article has been published as:

Dirac nodal lines protected against spin-orbit interaction in IrO_{2}

J. N. Nelson, J. P. Ruf, Y. Lee, C. Zeledon, J. K. Kawasaki, S. Moser, C. Jozwiak, E. Rotenberg, A. Bostwick, D. G. Schlom, K. M. Shen, and L. Moreschini

Phys. Rev. Materials **3**, 064205 — Published 18 June 2019

DOI: 10.1103/PhysRevMaterials.3.064205

Dirac nodal lines protected against spin-orbit interaction in IrO_2

J. N. Nelson,[1] J. P. Ruf,[1] Y. Lee,[1] C. Zeledon,[2] J. K. Kawasaki,[3] S. Moser,[4] C. Jozwiak,[5]
E. Rotenberg,[5] A. Bostwick,[5] D. G. Schlom,[2,6] K. M. Shen,[1,6,*] and L. Moreschini[2,†]
[1]*Laboratory of Atomic and Solid State Physics, Department of Physics, Cornell University, Ithaca, New York 14853, USA*
[2]*Department of Materials Science and Engineering, Cornell University, Ithaca, New York 14853, USA*
[3]*Department of Materials Science and Engineering, University of Wisconsin, Madison, Wisconsin 53706, USA*
[4]*Physikalisches Institut, Universität Würzburg, D-97074 Würzburg, Germany*
[5]*Advanced Light Source, Lawrence Berkeley National Laboratory, Berkeley, California 94720, USA*
[6]*Kavli Institute at Cornell for Nanoscale Science, Ithaca, New York 14853, USA*

The interplay between strong spin-orbit coupling and electron correlations has recently been the subject of intense investigation, due to a number of theoretically predicted phases such as quantum spin liquids, unconventional superconductivity, complex magnetic orders, and correlated topological phases of matter. In particular, iridates have been proposed as a promising family of materials which could host a number of these new phases. Here, we report the existence of Dirac nodal lines in the binary oxide IrO_2, through a combination of reactive oxide molecular beam epitaxy and angle-resolved photoemission spectroscopy. Unlike other such materials reported to date, these Dirac nodal lines have the unique property of being simultaneously i) robust against spin-orbit coupling, as they are protected by the nonsymmorphic symmetry of the rutile structure, and ii) only partially occupied, since they cross the Fermi level. This should have direct implications on the low-energy physics properties tied to the band velocity such as magnetoresistance and spin Hall effect.

I. INTRODUCTION

Transition metal oxides have been widely studied over the past three decades owing to their unprecedented variety of electronic and magnetic properties including high temperature and unconventional superconductivity, metal-insulator transitions, multiferroicity, and colossal magnetoresistance, which arise due to electron correlations between partially filled d orbitals [1]. Despite their heterogeneity, few oxides have been shown to harbor unusual topological properties. Indeed, the vast majority of topological insulators, Dirac semimetals and Weyl semimetals have been reported in intermetallic compounds [2–5], where calculations based on density functional theory (DFT) generally provide an accurate description of the electronic structure. It has been a major goal in condensed matter to achieve topological states where the topological protection is combined with the complex electronic and magnetic orders often present in oxides.

In this respect, iridates have been one of the main targets of investigation. As notable examples, the $R_2Ir_2O_7$ pyrochlores, where R is a rare-earth element, have been proposed to be Weyl semimetals or, under some conditions, axion insulators [6], while $SrIrO_3$ is predicted to be a topological crystalline metal with nodal rings [7]. Na_2IrO_3 and Li_2IrO_3 could provide the realization of the Kitaev quantum spin liquid model, which would harbor topological excitations such as Majorana fermions [8, 9]. Finally, Sr_2IrO_4 has been demonstrated to be a spin-orbit-assisted Mott insulator [10] with intriguing similarities to the cuprate superconductors [11, 12]. Nevertheless, the topological properties of many of these iridates remain difficult to identify, due in large part to the combination of spin-orbit and Coulomb interactions which makes first-principle calculations challenging, and to this point there exist no iridate compound whose topological nature has been conclusively determined.

The electronic structure of the rutile oxide IrO_2 has been relatively poorly studied by angle-resolved photoemission spectroscopy (ARPES) in comparison to other members of the family. The shortage of photoemission data is due in particular to the challenges in preparing high quality single crystals and to the lack of a natural cleavage plane. Like other iridates, IrO_2 also exhibits a number of interesting properties including a large spin Hall effect [13], a Hall effect where the carriers can be switched from electrons to holes by an applied magnetic field [14], as well as being an efficient catalyst [15, 16]. It shares with the rest of the family the fundamental building blocks, the IrO_6 octahedra with the Ir^{4+} ion in a $5d^5$ configuration, which in IrO_2 are connected in a combination of corner- and edge-sharing neighbors [Fig. 1(a)]. It was recently predicted by Sun *et al.* to host band crossings protected along continuous lines in reciprocal space, called Dirac nodal lines (DNLs) [17], which in general result from a combination of time-reversal symmetry and crystal symmetries [18]. While in the majority of cases the theoretically predicted DNLs are not realized in practice due to spin orbit coupling (SOC) opening a gap at the crossing point, in IrO_2 the nonsymmorphic symmetry of the crystal protects the band degeneracy along the nodal lines.

II. METHODS

A. Film growth, characterization and ARPES measurements

This study is a combination of reactive oxide molecular-beam epitaxy (MBE) synthesis and ARPES. In order to reveal the nodal lines along multiple directions in the reciprocal space, thin films were grown on different surfaces.

---

[*] kmshen@cornell.edu
[†] lmoreschini@cornell.edu

Epitaxial (110) and (001) oriented IrO_2 films were grown on single-crystal TiO_2 (110) and (001) substrates respectively [see Fig. 1(b) for an x-ray diffraction Cu Kα $\theta/2\theta$ scan, demonstrating high crystalline quality of both films]. Samples between 5 and 20 nm were grown at 300 °C in a background pressure of 1×10^{-6} distilled ozone. Immediately after growth a single monolayer of crystalline TiO_2 ($\sim$1.5 Å) was deposited as a protective cap under the same conditions. Samples were transported in low vacuum and annealed at 350 °C in 2×10^{-5} torr of 10% ozone prior to measurement. This process removes adsorbed contaminants from the surface, but does not remove the TiO_2 cap, as demonstrated by the post annealing x-ray photoemission spectroscopy (XPS) data shown in Fig. S3. The XPS Ti $2p$ signal is expected to originate from the overlayer only since all samples had a thickness of at least 5 nm, much larger than the inelastic mean free path of electrons at a kinetic energy of 600 eV [19]. Note that since TiO_2 has a wide band gap [20, 21] we do not expect to see in photoemission any contribution from the overlayer in the vicinity of the Fermi level. Further details on the film growth and characterization are available in Ref. 22.

ARPES measurements over the full three dimensional (3D) Brillouin zone (BZ) were undertaken at the MAESTRO beamline at the Advanced Light Source using a photon energy of 84-140 eV, with a combined resolution of 15 to 25 meV depending on the photon energy, at temperatures of approximately 70 K. For the experimental geometry see Fig. S5 in Ref. 22.

B. DFT calculations

Non-magnetic DFT calculations were performed using the Quantum ESPRESSO software package [23] using fully relativistic, norm-conserving pseudopotentials for Ir and O [24]. We represented the Kohn-Sham wavefunctions in a basis set of plane waves extending up to a kinetic energy cutoff of 80 Ry, and used a cutoff of 320 Ry for representing the charge density. An $8 \times 8 \times 12$ k-mesh was used for Brillouin zone integrations along with Gaussian smearing for band occupations. Perdew-Burke-Ernzerhof parametrization of the generalized gradient approximation (GGA) was employed as the exchange-correlation functional [25]. To ensure that our calculations accurately capture the effects of sizable spin-orbit coupling inherent to iridates, we cross-checked these results against those computed using the full-potential (linearized augmented plane wave plus local orbitals) WIEN2k code [26] and observed negligible differences in the band energies near the Fermi level. After obtaining self-consistent Kohn-Sham eigenstates via DFT, we used the Pw2wannier and Wannier90 codes [27] to construct 20 Wannier functions spanning the manifold of eigenstates surrounding E_F (10 d orbitals per Ir atom times 2 Ir atoms per unit cell).

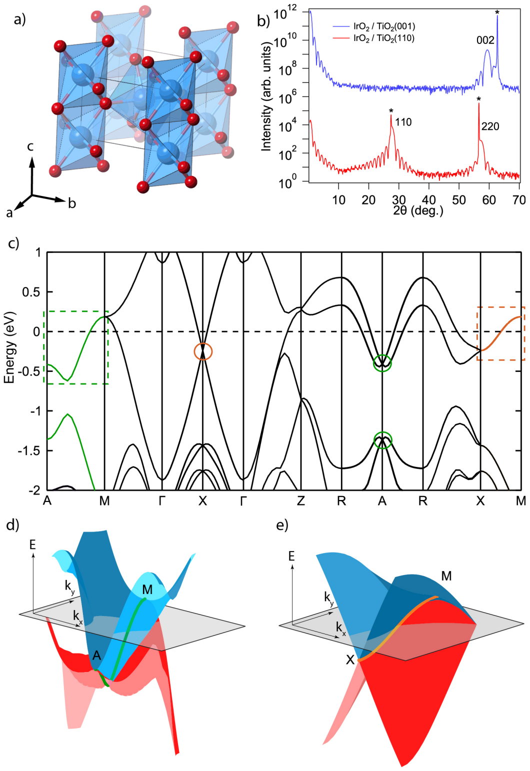

FIG. 1. (a) crystal structure of IrO_2 and (b) X-ray diffraction 2θ scans exhibiting clear thickness fringes from $\sim$15 nm thick IrO_2 (110) and IrO_2 (001) films. The asterisks mark the TiO_2 substrate peaks. (c) the calculated band structure by GGA+SOC along a selected high symmetry path. The nodal lines discussed in this work are marked by the dashed boxes. The Γ-X and R-A directions normal to the lines are shown twice for representing the characteristic Dirac crossings, marked by circles superposed to the band structure. Every path perpendicular to the DNLs will show such a a crossing point, as apparent in the 3D renderings of the band structure along A-M (d) and X-M (e) where the gray planes represent the location of the Fermi level. The higher binding energy nodal line along A-M is not focus of this work. It is not relevant for the low energy physics since it lies >1 eV from the Fermi level, and is likely to be difficult to measure accurately due to the broader ARPES linewidth at higher binding energy.

III. RESULTS

A. Crystal symmetry and electronic structure

Figure 1(c) shows the band structure along selected high symmetry directions, as obtained by DFT in the GGA approximation including SOC. The results are consistent with the band structure published in Refs. 17 and 28. Along A-M and X-M the dispersion consists of a single curve, where for space group n.136 a nonsymmorphic term adds an additional symmetry to the usual time and space inversions, and as a consequence the band degeneracy increases from double to fourfold. Namely, the combination of a translation of half the body diagonal τ and a fourfold rotational symmetry around the c axis provides the degeneracy along A-M [Fig. 1(d)], while the combination of τ and mirror symmetry with respect to the a

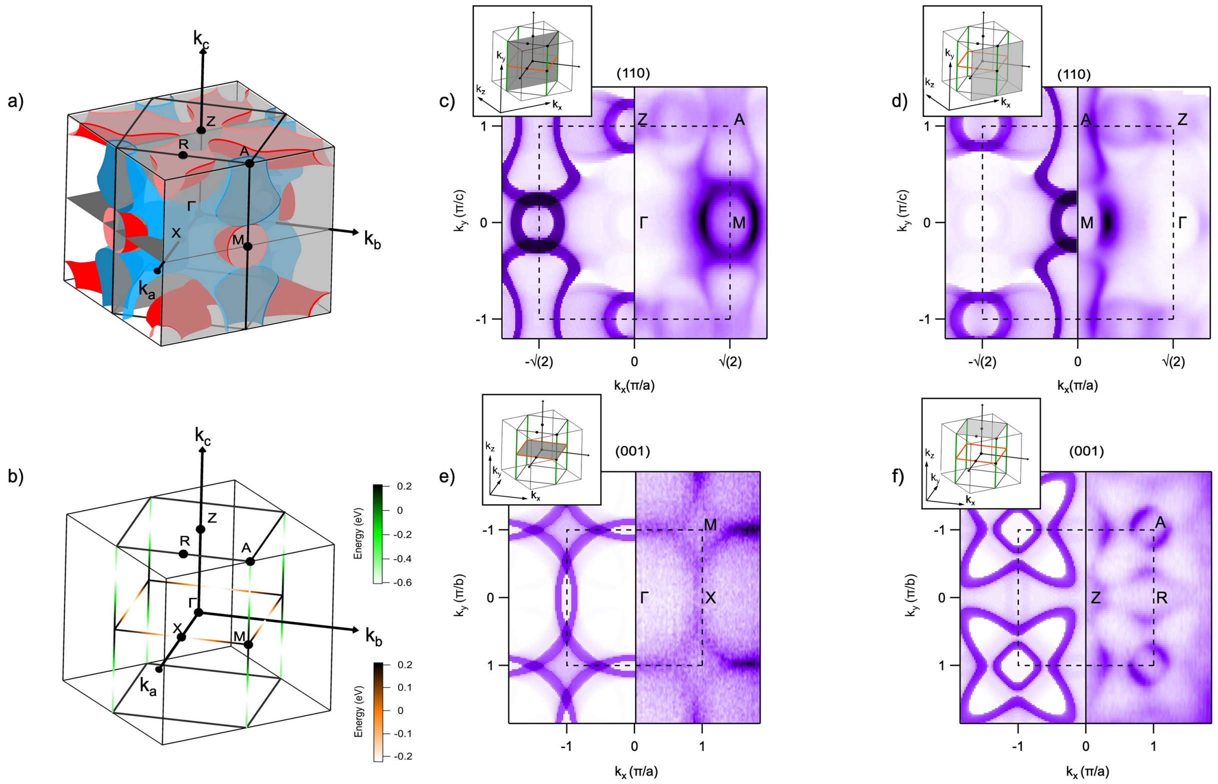

FIG. 2. (a) 3D rendering of the calculated Fermi surface, with hole-like bands in red and electron-like bands in blue. The grey planes correspond to the BZ center and BZ boundary for the [110] and [001] orientations, and indicate the location of the Fermi surfaces measured by ARPES in (c-f), as shown in the insets. (b) The 3D BZ with high symmetry directions hosting the DNLs object of this study, shown in green for the A-M line and orange for the X-M line. The energy of the band along the k path is color coded as shown. The photon energies used are (c) 124 eV, (d) 84 eV, (e) 140 eV and (f) 100 eV, and the inner potential V_0 used is 11.5 eV for (110) and 4 eV for (001) films, respectively. The sample temperature was ∼70 K. On the left half of (c-f), the calculated Fermi surfaces are shown with a k_z broadening of 0.2 Å^{-1}. For bulk IrO_2 , $\pi/a = \pi/b \simeq 0.70$ Å^{-1}, $\pi/c \simeq 1.00$ Å^{-1}. The experimental data show a slight mismatch with the drawn bulk BZs in view of the strain on films. In all ARPES plots and in the text we name xy the sample surface plane and z the axis normal, for both orientations. As a consequence, k_z is the out of plane momentum regardless of the surface.

axis is responsible for that along X-M [Fig. 1(e)].

B. Comparison to DFT

The choice of the sample orientation for measuring the DNLs is in principle arbitrary, but because of the strong photon energy dependence of the photoemission intensity in IrO_2 we choose to measure A-M and X-M on the (110) and (001) surface, respectively, where they can be followed at constant $h\nu$.

The calculated 3D Fermi surface is shown in Fig. 2(a), and consists of two sheets of hole-like states (red) and one of electron-like states (blue). The reciprocal space locations of the nodal lines are shown in Fig. 2(b), with the A-M line in green and the X-M line in orange, the latter forming closed loops. It is apparent that the A-M line is more naturally accessible by ARPES on the (110) surface, as the whole line can be measured at a single photon energy, while the X-M line is more easily measured on the (001) surface. This motivates the synthesis and measurement of these two orientations of IrO_2. In figures 2(c,d) and 2(e,f) we show the measured Fermi surfaces for (110) and (001) films, respectively, at the center (c,e) and at the boundary (d,f) of the BZ, compared to simulated Fermi surface maps from DFT with an added k_z broadening of 0.2 Å^{-1}. Aside from a slight discrepancy between the relative sizes of the hole and electron pockets in the (110) surface, the experimental results match with the DFT predictions, with no observable surface states as opposed to what previously claimed [29] (this point is further clarified in Fig. S4). Considering the importance of correlations in partially filled d orbitals, it is not *a priori* guaranteed that a DFT approach is a good starting point, and therefore the presence of such agreement is not a trivial observation.

The results shown in Fig. 2(c,d) are consistent with earlier ARPES measurements on IrO_2 (110) [28, 29], though the present data are the most extensive to date and the first ones on IrO_2(001). In regards to these constant energy maps, it is worthwhile to note that the ARPES intensity is fairly isotropic with p polarization, but shows a clear suppression in s polarization along the k_x and k_y axes, as we show in Fig. S5 for the Fermi surface measured on (110) at the M point. This is

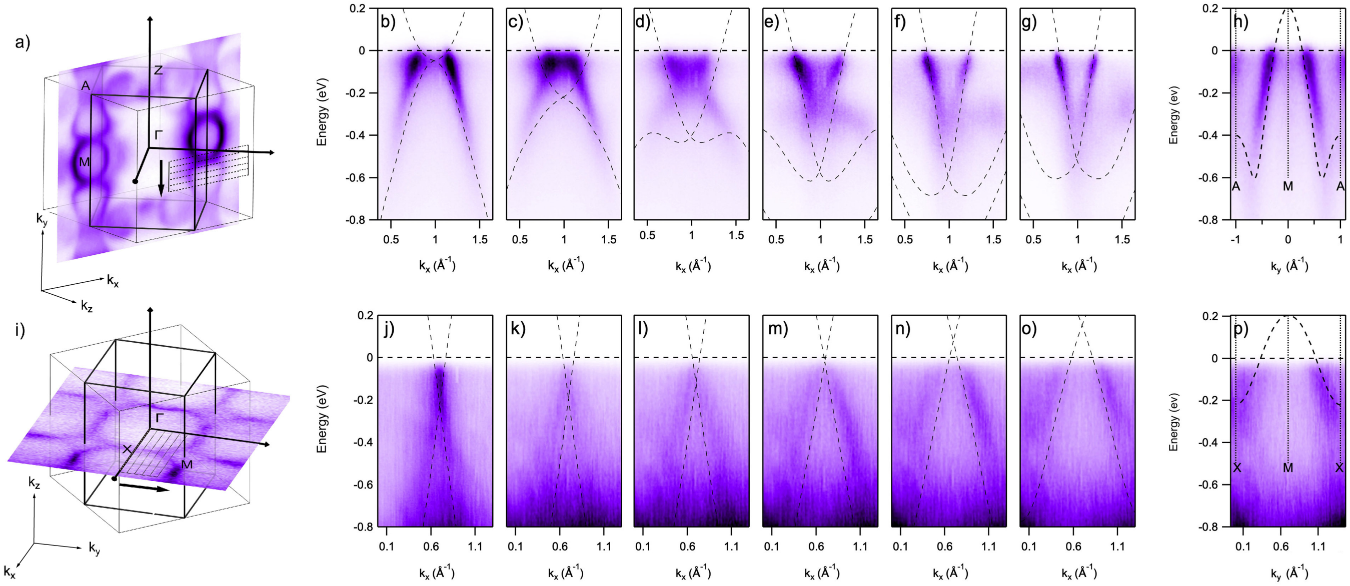

FIG. 3. (a) The Fermi surface for the (110) surface at the BZ center, from Fig. 2(b). The dashed lines and the arrow indicate the locations of the dispersion images for the data in (b-g), where the DFT results are superposed as dashed curves. (i) and (j-o) are the equivalent of (a) and (b-g) for the (001) surface. (h) and (p) show the nodal line dispersion along A-M-A and X-M-X, respectively. The sample temperature was ∼70 K. The photon energy is 124 eV for A-M and 140 eV for X-M.

immediate consequence of some degree of orbital ordering in IrO_2 [30], as opposed to the perovskite iridates where the orbital momentum L is not a good quantum number and ARPES shows no dipole matrix element effects [10]. The minor role of correlations in IrO_2 in comparison with other iridates is believed to stem from the different arrangement and higher connectivity of the octahedra in the rutile structure [28, 30].

C. Evolution of the nodal lines

In Fig. 3 we focus more directly on the measurement of the nodal lines, starting from the A-M direction in the (110) sample. In Fig. 3(a), the Fermi surface of Fig. 2(c) is inserted in the 3D BZ. The dashed lines mark the locations of the E *vs* k_x images (with k_x normal to the plane containing the DNL) shown in Fig. 3(b-g), in direction of M to A as indicated by the arrow. The ensuing nodal line dispersion is shown in the E *vs* k_y image of Fig. 3(h). The DFT bands are superposed to the data for clarity. Near M the electronic states are unoccupied as the Fermi surface consists of a hole pocket. Taking cuts in direction of A, the crossing point moves to and below the Fermi level. The band dispersion in the vicinity of the crossing point becomes less clear towards A where it is further from the Fermi level. Because of the aforementioned underestimation of the hole pockets the theory agrees with the data but with a mismatch in the binding energy of the crossing point (the mismatch is large enough that the Fermi level crossing of the Dirac node in DFT is outside the range shown here for the A-M line). Fig. 3(j-o) are the correspondent of the top panels, now for the X-M line, with the Fermi surface from Fig. 2(e) inserted in Fig. 3(i). The Fermi surface is slightly electron-like at X, with a crossing point at ∼50 meV binding energy, and evolves into the hole-like sheet at M. The nodal line dispersion is shown Fig. 3(p). The band dispersion at the crossing points is not guaranteed to be linear over a large energy range, and while in some cases a roughly linear dispersion extends over more than 1 eV [31], in others the dispersion has a higher order term at all energies [32]. In IrO_2 the linear dispersion is clearly visible over several hundreds of meV only along X-M, while along A-M the bands appear parabolic all the way to the crossing point.

Within the limitations dictated by the experimental broadening of the linewidth, we cannot find the presence of any gap in either nodal line. Also the dispersion along R-A-R measured on the (001) surface, where the dispersion can be more easily followed, clearly hints at a gapless crossing at A (see Fig. S6). On this point, note that, as opposed to the many instances of quasi 2D materials hosting Dirac crossings, more sophisticated analysis methods aiming to exclude the presence of a gap in bulk states of 3D systems do not seem, in general, justified. Due to the finite escape depth of photoelectrons, ARPES data present an intrinsic k_z broadening. Using a reasonable value of $\lambda = 5$ Å for the electron mean free path, we obtain an approximate k_z distribution over $1/\lambda = 0.2$ Å^{-1} [33]. For IrO_2, along both nodal lines, at a k_z value 0.1 Å^{-1} away from the Dirac node, a gap larger than 50 meV is expected (see Fig. S7). The strict identification of a crossing point in bulk states is therefore not possible, and the presence of a single peak depends on the exact k_z dispersion in the vicinity of the node and on other (extrinsic) broadening factors. In addition to the above, whereas growth on the (001) surface preserves the space group symmetry, in (110) films the surface epitaxial strain distorts the rutile structure, breaking the symmetry terms which protect the nodal lines. For a unit cell distortion by ∼2% along $[1\bar{1}0]$, ∼-5% along [001] and ∼0.8% along [110] (normal to the surface plane), as inferred by x-ray diffraction (see Ref. 22), DFT predicts an opening of a gap as large as ∼50 meV depending on the parallel momentum, as shown in Fig. S9.

IV. DISCUSSION

There is an apparent difference between the electronic structure of IrO_2 and that of the other DNL materials reported so far. Both nodal lines here have a large energy dispersion (∼0.5 eV) and they cross the Fermi level, making it a unique case. As an immediate consequence, any contribution to the low energy physics can be expected to be robust against perturbations which shift the chemical potential.

Nodal lines may be categorized on the basis of which symmetry terms are at their origin, with some compounds believed to host more than a single type. When time reversal symmetry is required for its existence, by definition the nodal line is not robust against SOC. The lifting of the degeneracy can be minor in materials with a small spin-orbit term [34–36], but dramatic in those containing heavy elements [37, 38]. Protection from SOC requires an additional symmetry other than space inversion, namely a nonsymmorphic term in the crystal space group [18] (a separate case is the one of Weyl nodal lines, which are protected by mirror symmetry and where the spin components are split by broken time or space inversion symmetry [39]). The accepted examples of DNLs protected by nonsymmorphic symmetry are mostly found in crystals of the $P4/nmm$, n.129 space group, namely the family of Zr(Hf)SiX compounds, (X=S, Se, Te) [31, 40–42] and InBi [43], whereas IrO_2 crystallizes in space group n.136. A number of others have been predicted [44, 45] but not yet experimentally verified.

In contrast to IrO_2, however, both in InBi and in the Zr(Hf)SiS family the nonsymmorphic symmetry protected DNL along X-R is far below the Fermi level, making it out of reach for low energy excitations [43, 46]. The nodal lines lying on the natural (001) cleaving plane, on the other hand, show a small dispersion along the characteristic diamond-shaped Fermi surface and are unstable against SOC, with a gap opening from ∼20 meV to several tens of meV depending on the spin-orbit term of the atomic species in the crystal. In Zr(Hf)SiTe the X-R line is instead believed by theory to lie much closer to the Fermi level, but it could not be seen in experiments, possibly because of natural hole doping in this family of layered crystals [42].

A separate mention deserves the case of RuO_2, which is isostructural to IrO_2 and was recently found to host a nodal line along the X-R high symmetry direction, crossing the Fermi level [47]. Although there is no symmetry protection along X-R, the small SOC of Ru (∼0.13 eV *vs* ∼0.41 eV) relative to Ir [48], together with the obligated fourfold degeneracy at X, makes it so that the gap is only a few meV in the vicinity of X, where the Fermi level crossing occurs. This provides a useful term of comparison between a material with low energy states consisting of a DNL strictly protected against SOC, and one with a very similar band structure but with lifted degeneracy, albeit by a small gap. How much influence such perturbation may have on the low energy properties is an open question, and it is argued by several authors that in materials with light elements the effect of SOC on the DNL could be considered in practice negligible [34, 36].

The comparison is particularly relevant between IrO_2 and RuO_2 since the two are widely studied in electrochemistry for water splitting. In $RuO_2(110)$ a surface state pinned to the nodal line was observed, but its role for photocatalysis remains uncertain since IrO_2 shows a similar activity ratio [49] but does not host any surface state. Also, the influence on chemistry of the details of the band structure at a given orientation seems difficult to reconcile with the higher efficiency reported in amorphous compared to rutile RuO_2 films [50].

IrO_2 was shown to exhibit large magnetoresistance [51, 52], for which a key quantity is the electron mobility, and therefore the band velocity. It is difficult to infer a reliable Fermi velocity for the A-M DNL where the carriers are massive except for a small region around the crossing point. In contrast, the band velocity in the X-M DNL along the Γ-X direction is linear over a large range [Fig. 3(j)], and we extract $hv_F \simeq 3.1$ eV·Å, a large value, higher than ∼2 eV·Å in RuO_2 [47], comparable to ∼3-5 eV·Å for the Dirac crossing at X in Zr(Hf)SiS [31, 42] and about half of ∼6.5 eV·Å in graphene [53]. These considerations altogether hint at the possibility that IrO_2 may be a viable candidate for magnetoresistive devices. However, the large variations observed within the different DNL compounds – the magnetoresistance in IrO_2 [51, 52] is larger than in good conductors such as noble or alkali metals [54], but at least two orders of magnitude smaller than in ZrSiS [55, 56], and at least three orders of magnitude smaller than in the WP_2 and MoP_2 Weyl semimetals [54], all layered, quasi-2D compounds – clearly indicates that the presence of massless fermions is not linked to the magnetotransport properties in a straightforward way and is instead strongly dependent on the fermiology of the material.

This work has shown that the binary oxide IrO_2 has an exotic electronic structure consisting of a network of intersecting nodal lines along A-M and X-M where the band crossings are protected by nonsymmorphic symmetry against strong SOC. These nodal lines are unusual in that they disperse strongly in energy and cross the Fermi level. Some aspects make IrO_2 a non trivial target for further work aiming to tune and explore new topological properties. The rutile structure is more three dimensional and therefore i) has a more complex fermiology, and ii) is less prone to modular heterostructuring where electronic properties can be altered and engineered with strain and confinement, with respect to layered compounds such as perovskites. In view of studying the interplay of SOC-driven topological phases and correlations [6], it lies in the weak correlation limit due to the large (∼3 eV) bandwidth of its t_{2g} states. Nonetheless, aside from the important differences established above with respect to the DNL compounds discovered so far, IrO_2 is an exciting playground for this field in that it is a simple binary transition metal oxide, already widely studied for practical applications. It can be grown epitaxially at low temperatures, making it suitable for integration in more complex architectures. This is in contrast to the other iridates, which have complex crystal structures and are in general difficult to synthesize. A fascinating direction to pursue in the future is to identify clearer connections between the band structure of IrO_2 and its macroscopic properties such as the large spin Hall effect or magnetoresistance, or yet its efficiency in catalysis. There are no established links between these at the moment, and working on epitaxial films allows for additional tuning parameters by exposing different crystal planes and imparting strain. As an example, it is an interesting question, which requires further investigation, how sizeable the effect of the crystal distortion in the (110) orientation is on the low energy properties such as the large spin Hall effect [13]. Recent work on the predicted nodal line material $SrIrO_3$, for example, points to a determinant role played by the nonsymmoprhic symmetry term, in lack of which, such as under epitaxial strain, the spin Hall conductivity decreases [57].

ACKNOWLEDGMENTS

We gratefully acknowledge discussions with Alberto Crepaldi, Christian R. Ast and Jin Suntivich. L. M. thanks Helmut Berger, Arnaud Magrez and Philippe Bugnon for providing IrO_2 single crystals for preliminary measurements. This work was supported through the National Science Foundation [Platform for the Accelerated Realization, Analysis, and Discovery of Interface Materials (PARADIM)] under Cooperative Agreement No. DMR-1539918, NSF DMR-1709255, and the Air Force Office of Scientific Research Grant No. FA9550-15-1-0474. J. N. N. acknowledges support from the NSF Graduate Research Fellowship under Grant No. DGE-1650441. This research used resources of the Advanced Light Source, which is a DOE Office of Science User Facility under Contract No. DE-AC02-05CH11231. This work made use of the Cornell Center for Materials Research Shared Facilities which are supported through the NSF MRSEC program (DMR-1719875). Substrate preparation was performed in part at the Cornell NanoScale Facility, a member of the National Nanotechnology Coordinated Infrastructure (NNCI), which is supported by the NSF (Grant No. ECCS-1542081). Some images were generated using CrystalMaker®: CrystalMaker Software Ltd. (www.crystalmaker.com).

Note added: after submission of this work, another article appeared on IrO_2(110) single crystals, in qualitative agreement with most of our findings [58].

---

[1] J. Ngai, F. Walker, and C. Ahn, Annual Review of Materials Research **44**, 1 (2014).

[2] Y. Liu, L. Yu, X. Jia, J. Zhao, H. Weng, Y. Peng, C. Chen, Z. Xie, D. Mou, J. He, X. Liu, Y. Feng, H. Yi, L. Zhao, G. Liu, S. He, X. Dong, J. Zhang, Z. Xu, C. Chen, G. Cao, X. Dai, Z. Fang, and X. J. Zhou, Scientific reports **40506**, 5 (2014).

[3] M. Neupane, S.-Y. Xu, R. Sankar, N. Alidoust, G. Bian, C. Liu, I. Belopolski, T.-R. Chang, H.-T. Jeng, H. Lin, A. Bansil, F. Chou, and M. Z. Hasan, Nature Communications **5**, 3786 EP (2014).

[4] J. A. Logan, S. J. Patel, S. D. Harrington, C. M. Polley, B. D. Schultz, T. Balasubramanian, A. Janotti, A. Mikkelsen, and C. J. Palmstrøm, Nature Communications **7**, 11993 (2016).

[5] Z. K. Liu, L. X. Yang, S. C. Wu, C. Shekhar, J. Jiang, H. F. Yang, Y. Zhang, S. K. Mo, Z. Hussain, B. Yan, C. Felser, and Y. L. Chen, Nature Communications **7**, 12924 (2016).

[6] W. Witczak-Krempa, G. Chen, Y. B. Kim, and L. Balents, Ann. Rev. of Cond. Matter Phys. **5**, 57 (2014).

[7] J.-M. Carter, V. V. Shankar, M. A. Zeb, and H.-Y. Kee, Phys. Rev. B **85**, 115105 (2012).

[8] S. Hwan Chun, J.-W. Kim, J. Kim, H. Zheng, C. C. Stoumpos, C. D. Malliakas, J. F. Mitchell, K. Mehlawat, Y. Singh, Y. Choi, T. Gog, A. Al-Zein, M. M. Sala, M. Krisch, J. Chaloupka, G. Jackeli, G. Khaliullin, and B. J. Kim, Nature Physics **11**, 462 EP (2015).

[9] T. Takayama, A. Kato, R. Dinnebier, J. Nuss, H. Kono, L. S. I. Veiga, G. Fabbris, D. Haskel, and H. Takagi, Phys. Rev. Lett. **114**, 077202 (2015).

[10] B. J. Kim, H. Jin, S. J. Moon, J.-Y. Kim, B.-G. Park, C. S. Leem, J. Yu, T. W. Noh, C. Kim, S.-J. Oh, J.-H. Park, V. Durairaj, G. Cao, and E. Rotenberg, Phys. Rev. Lett. **101**, 076402 (2008).

[11] Y. K. Kim, O. Krupin, J. D. Denlinger, A. Bostwick, E. Rotenberg, Q. Zhao, J. F. Mitchell, J. W. Allen, and B. J. Kim, Science **345** (2014).

[12] Y. K. Kim, N. H. Sung, J. D. Denlinger, and K. BJ, Nature Physics **12**, 1 (2015).

[13] K. Fujiwara, Y. Fukuma, J. Matsuno, H. Idzuchi, Y. Niimi, Y. Otani, and H. Takagi, Nature Communications **4**, 2893 (2013).

[14] M. Uchida, W. Sano, K. S. Takahashi, T. Koretsune, Y. Kozuka, R. Arita, Y. Tokura, and M. Kawasaki, Phys. Rev. B **91**, 241119(R) (2015).

[15] D.-Y. Kuo, J. K. Kawasaki, J. N. Nelson, J. Kloppenburg, G. Hautier, K. M. Shen, D. G. Schlom, and J. Suntivich, Journal of the American Chemical Society **139**, 3473 (2017).

[16] Z. Liang, T. Li, M. Kim, A. Asthagiri, and J. F. Weaver, Science **356**, 299 (2017).

[17] Y. Sun, Y. Zhang, C.-X. Liu, C. Felser, and B. Yan, Phys. Rev. B **95**, 235104 (2017).

[18] S.-Y. Yang, H. Yang, E. Derunova, S. S. P. Parkin, B. Yan, and M. N. Ali, Advances in Physics: X **3**, 1414631 (2018).

[19] M. P. Seah and W. Dench, Surface and Interface Analysis **1** (1979).

[20] S. U. M. Khan, M. Al-Shahry, and W. B. Ingler, Science **297**, 2243 (2002).

[21] S.-D. Mo and W. Y. Ching, Phys. Rev. B **51**, 13023 (1995).

[22] Supplementary information is attached to this paper. It includes data on sample characterization, polarization-dependent ARPES data and a study of the effects of strain.

[23] P. Giannozzi, S. Baroni, N. Bonini, M. Calandra, R. Car, C. Cavazzoni, D. Ceresoli, G. L. Chiarotti, M. Cococcioni, I. Dabo, A. Dal Corso, S. de Gironcoli, S. Fabris, G. Fratesi, R. Gebauer, U. Gerstmann, C. Gougoussis, A. Kokalj, M. Lazzeri, L. Martin-Samos, N. Marzari, F. Mauri, R. Mazzarello, S. Paolini, A. Pasquarello, L. Paulatto, C. Sbraccia, S. Scandolo, G. Sclauzero, A. P. Seitsonen, A. Smogunov, P. Umari, and R. M. Wentzcovitch, Journal of Physics: Condensed Matter **21**, 395502 (2009).

[24] D. R. Hamann, Physical Review B **88**, 085117 (2013).

[25] J. P. Perdew, K. Burke, and M. Ernzerhof, Physical Review Letters **77**, 3865 (1996).

[26] P. Blaha, K. Schwarz, G. K. H. Madsen, D. Kvasnicka, J. Luitz, R. Laskowski, F. Tran, and L. D. Marks, *WIEN2k, An Augmented Plane Wave + Local Orbitals Program for Calculating Crystal Properties* (Karlheinz Schwarz, Vienna University of Technology, Austria, 2018).

[27] A. A. Mostofi, J. R. Yates, G. Pizzi, Y.-S. Lee, I. Souza, D. Vanderbilt, and N. Marzari, Computer Physics Communications **185**, 2309 (2014).

[28] J. K. Kawasaki, M. Uchida, H. Paik, D. G. Schlom, and K. M. Shen, Phys. Rev. B **94**, 121104(R) (2016).

[29] P. K. Das, J. Sławińska, I. Vobornik, J. Fujii, A. Regoutz, J. M. Kahk, D. O. Scanlon, B. J. Morgan, C. McGuinness, E. Plekhanov, D. Di Sante, Y.-S. Huang, R.-S. Chen, G. Rossi, S. Picozzi, W. R. Branford, G. Panaccione, and D. J. Payne, Phys. Rev. Materials **2**, 065001 (2018).

[30] J. M. Kahk, C. G. Poll, F. E. Oropeza, J. M. Ablett, D. Céolin, J.-P. Rueff, S. Agrestini, Y. Utsumi, K. D. Tsuei, Y. F. Liao, F. Borgatti, G. Panaccione, A. Regoutz, R. G. Egdell, B. J. Morgan, D. O. Scanlon, and D. J. Payne, Phys. Rev. Lett. **112**, 117601 (2014).

[31] L. M. Schoop, M. N. Ali, C. Straßer, A. Topp, A. Varykhalov, D. Marchenko, V. Duppel, S. S. P. Parkin, B. V. Lotsch, and C. R. Ast, Nature Communications **7**, 11696 (2016).

[32] N. P. Armitage, E. J. Mele, and A. Vishwanath, Rev. Mod. Phys. **90**, 015001 (2018).

[33] V. Strocov, Journal of Electron Spectroscopy and Related Phenomena **130**, 65 (2003).

[34] L. S. Xie, L. M. Schoop, E. M. Seibel, Q. D. Gibson, W. Xie, and R. J. Cava, APL Materials **3**, 083602 (2015).

[35] E. Emmanouilidou, B. Shen, X. Deng, T.-R. Chang, A. Shi, G. Kotliar, S.-Y. Xu, and N. Ni, Phys. Rev. B **95**, 245113 (2017).

[36] B. Feng, B. Fu, S. Kasamatsu, S. Ito, P. Cheng, C.-C. Liu, Y. Feng, S. Wu, S. K. Mahatha, P. Sheverdyaeva, P. Moras, M. Arita, O. Sugino, T.-C. Chiang, K. Shimada, K. Miyamoto, T. Okuda, K. Wu, L. Chen, Y. Yao, and I. Matsuda, Nature communications **8**, 1007; 1007 (2017).

[37] R. Yu, Q. Wu, Z. Fang, and H. Weng, Phys. Rev. Lett. **119**, 036401 (2017).

[38] Q. Xu, Z. Song, S. Nie, H. Weng, Z. Fang, and X. Dai, Phys. Rev. B **92**, 205310 (2015).

[39] G. Bian, T.-R. Chang, R. Sankar, S.-Y. Xu, H. Zheng, T. Neupert, C.-K. Chiu, S.-M. Huang, G. Chang, I. Belopolski, D. S. Sanchez, M. Neupane, N. Alidoust, C. Liu, B. Wang, C.-C. Lee, H.-T. Jeng, C. Zhang, Z. Yuan, S. Jia, A. Bansil, F. Chou, H. Lin, and M. Z. Hasan, Nature Communications **7**, 10556 (2016).

[40] M. Neupane, I. Belopolski, M. M. Hosen, D. S. Sanchez, R. Sankar, M. Szlawska, S.-Y. Xu, K. Dimitri, N. Dhakal, P. Maldonado, P. M. Oppeneer, D. Kaczorowski, F. Chou, M. Z. Hasan, and T. Durakiewicz, Phys. Rev. B **93**, 201104(R) (2016).

[41] D. Takane, Z. Wang, S. Souma, K. Nakayama, C. X. Trang, T. Sato, T. Takahashi, and Y. Ando, Phys. Rev. B **94**, 121108(R) (2016).

[42] A. Topp, J. M. Lippmann, A. Varykhalov, V. Duppel, B. V. Lotsch, C. R. Ast, and L. M. Schoop, New J. Phys. **18**, 125014 (2018).

[43] S. A. Ekahana, S.-C. Wu, J. Jiang, K. Okawa, D. Prabhakaran, C.-C. Hwang, S.-K. Mo, T. Sasagawa, C. Felser, B. Yan, Z. Liu, and Y. Chen, New Journal of Physics **19**, 065007 (2017).

[44] G. Bian, T.-R. Chang, H. Zheng, S. Velury, S.-Y. Xu, T. Neupert, C.-K. Chiu, S.-M. Huang, D. S. Sanchez, I. Belopolski, N. Alidoust, P.-J. Chen, G. Chang, A. Bansil, H.-T. Jeng, H. Lin, and M. Z. Hasan, Phys. Rev. B **93**, 121113(R) (2016).

[45] S. Li, Y. Liu, S.-S. Wang, Z.-M. Yu, S. Guan, X.-L. Sheng, Y. Yao, and S. A. Yang, Phys. Rev. B **97**, 045131 (2018).

[46] C. Chen, X. Xu, J. Jiang, S.-C. Wu, Y. P. Qi, L. X. Yang, M. X. Wang, Y. Sun, N. B. M. Schröter, H. F. Yang, L. M. Schoop, Y. Y. Lv, J. Zhou, Y. B. Chen, S. H. Yao, M. H. Lu, Y. F. Chen, C. Felser, B. H. Yan, Z. K. Liu, and Y. L. Chen, Phys. Rev. B **95**, 125126 (2017).

[47] V. Jovic, R. J. Koch, S. K. Panda, H. Berger, P. Bugnon, A. Magrez, K. E. Smith, S. Biermann, C. Jozwiak, A. Bostwick, E. Rotenberg, and S. Moser, Phys. Rev. B **98**, 241101(R) (2018).

[48] K. V. Shanavas, Z. S. Popović, and S. Satpathy, Phys. Rev. B **90**, 165108 (2014).

[49] D.-Y. Kuo, H. Paik, J. Kloppenburg, B. Faeth, K. M. Shen, D. G. Schlom, G. Hautier, and J. Suntivich, Journal of the American Chemical Society **140**, 17597 (2018).

[50] E. Tsuji, A. Imanishi, K. ichi Fukui, and Y. Nakato, Electrochimica Acta **56**, 2009 (2011).

[51] W. D. Ryden, W. A. Reed, and E. S. Greiner, Phys. Rev. B **6**, 2089 (1972).

[52] J. J. Lin, S. M. Huang, Y. H. Lin, T. C. Lee, H. Liu, X. X. Zhang, R. S. Chen, and Y. S. Huang, Journal of Physics: Condensed Matter **16**, 8035 (2004).

[53] P. R. Wallace, Phys. Rev. **71**, 622 (1947).

[54] N. Kumar, Y. Sun, N. Xu, K. Manna, M. Yao, V. Süss, I. Leermakers, O. Young, T. Förster, M. Schmidt, H. Borrmann, B. Yan, U. Zeitler, M. Shi, C. Felser, and C. Shekhar, Nature Communications **8**, 1642 (2017).

[55] X. Wang, X. Pan, M. Gao, J. Yu, J. Jiang, J. Zhang, H. Zuo, M. Zhang, Z. Wei, W. Niu, Z. Xia, X. Wan, Y. Chen, F. Song, Y. Xu, B. Wang, G. Wang, and R. Zhang, Advanced Electronic Materials **2**, 1600228 (2016).

[56] R. Singha, A. K. Pariari, B. Satpati, and P. Mandal, Proceedings of the National Academy of Sciences **114**, 2468 (2017).

[57] T. Nan, T. J. Anderson, J. Gibbons, K. Hwang, N. Campbell, H. Zhou, Y. Q. Dong, G. Y. Kim, N. Reynolds, X. J. Wang, N. X. Sun, S. Y. Choi, M. S. Rzchowski, Y. B. Kim, D. C. Ralph, and C. B. Eom, arXiv:1808.06650.

[58] X. Xu, J. Jiang, W. J. Shi, V. Süß, C. Shekhar, S. C. Sun, Y. J. Chen, S.-K. Mo, C. Felser, B. H. Yan, H. F. Yang, Z. K. Liu, Y. Sun, L. X. Yang, and Y. L. Chen, Phys. Rev. B **99**, 195106 (2019) .